Materials Today Catalysis 7 (2024) 100076

Contents lists available at ScienceDirect

Materials Today Catalysis

journal homepage: www.journals.elsevier.com/materials-today-catalysis

MXene termination and stacking bias on the reverse water gas shift reaction catalysis

Ángel Morales-García [a,1], José D. Gouveia [b,1], Anna Vidal López [c], Aleix Comas-Vives [c,d], Francesc Viñes [a,*], José R.B. Gomes [b], Francesc Illas [a]

[a] Departament de Ciència de Materials i Química Física & Institut de Química Teòrica i Computacional (IQTCUB), Universitat de Barcelona, c/ Martí i Franquès 1-11, Barcelona 08028, Spain
[b] CICECO-Aveiro Institute of Materials, Department of Chemistry, University of Aveiro, Campus Universitário de Santiago, Aveiro 3810-193, Portugal
[c] Department of Chemistry, Universitat Autònoma de Barcelona, Catalonia, Cerdanyola del Vallès 08193, Spain
[d] Institute of Materials Chemistry, TU Wien, Vienna 1060, Austria

ARTICLE INFO

Keywords:
Molybdenum carbide MXenes
Stacking
Surface termination
Reverse water gas shift
Kinetics
Density functional theory
Microkinetic modeling

ABSTRACT

Pristine Mo_2C MXene has been recently highlighted as a highly active and robust catalyst for the reverse water gas shift (RWGS) reaction. Here, first-principles calculations based on density functional theory (DFT) coupled with mean-field microkinetic (MKM) simulations are performed to investigate the effects of the atomic layer stacking and the surface functionalization with oxo groups on the catalyst performance. The calculated data show that ABA stacked MXene has a reactivity higher than the corresponding ABC counterpart. Moreover, a $^2/_3$ surface monolayer oxygen coverage on both stackings (*i.e.*, $Mo_2CO_{4/3}$ MXene) enhances the overall reactivity compared with their pristine Mo_2C counterparts. The reactivity enhancement is small for the more stable ABA-stacked model, with a CO gas production aligned with experimental reports. However, the partial O-surface termination in the MXene with ABC stacking offers a more enhanced reactivity, supported by the higher CO gas production for the Mo_2C MXene models here considered. Thus, the MXene stacking and its functionalization are key aspects affecting the performance of the Mo_2C MXene for the RGWS reaction, which must be considered for realistic catalytic applications of MXenes.

1. Introduction

Anthropogenic carbon dioxide (CO_2) emissions are the main contributor to the greenhouse effect, given the ever-growing CO_2 concentration rise in the atmosphere during the last decades [1]. This causes severe environmental problems that threaten mankind, such as ocean acidification, global warming, and glaciers melting, to name a few [2,3]. Therefore, the reduction of CO_2 concentration is among the core action lines in any climate remediation agenda and has become one of the biggest challenges for the scientific community, with many research endeavors placed on carbon capture and storage (CCS) and utilization (CCU) technologies [4]. In principle, CCU-based technologies are more appealing than CCS since the former aim is to convert CO_2 into other valuable and ideally environmentally friendly chemicals [5].

Heterogeneous catalysts suited for CCU platforms are in high demand to achieve the planned targets of green and sustainable chemistry [6]. Among the different CO_2 upgrading processes [7], the reverse water gas shift (RWGS) reaction —$CO_2^{(g)} + H_2^{(g)} \rightarrow CO^{(g)} + H_2O^{(g)}$; $\Delta G^o = 0.3$ eV at temperature $T = 298.15$ K— is an appealing and viable route to obtain carbon monoxide (CO) from CO_2 using as reactant hydrogen (H_2), ideally employing H_2 gained using renewable energy sources, such as through the electrochemical water splitting using excess wind or sunlight power. Notably, the overall RWGS has water (H_2O) as the only by-product. The obtained CO can be subsequently used in the downstream Fischer-Tropsch (FT) reaction or methanol synthesis processes [8–11], again especially attractive when using *green* H_2. The endergonic nature of the RWGS requires high temperatures to achieve CO_2 conversion, and that is why it is peremptory to use highly active and selective catalysts to imbalance the C–O dissociation and hydrogenation steps as well as to operate under working conditions as mild as possible.

Usual RWGS catalysts consist of metal active sites, *i.e.*, Cu, Pt, Pd, or Rh, well dispersed on high-surface metal oxide supports, such as CeO_2,

* Corresponding author.
E-mail address: francesc.vines@ub.edu (F. Viñes).
[1] Contributed equally

https://doi.org/10.1016/j.mtcata.2024.100076
Received 30 September 2024; Received in revised form 11 November 2024; Accepted 17 November 2024
Available online 19 November 2024
2949-754X/© 2024 The Authors. Published by Elsevier Ltd. This is an open access article under the CC BY license (http://creativecommons.org/licenses/by/4.0/).

often used due to its excellent redox properties [12–15], or other oxides such as TiO_2 and ZnO [16,17]. Given the scarcity and high cost of the late transition metals, transition metal carbides (TMCs) have also been explored as efficient and more economic catalysts for the RWGS, in line with the similar activity of noble metals and poisoning resistance [18–20]. Indeed, TMCs have also been regarded as supports of transition metals for the RWGS, adjoining synergistic effects between metal and support [21].

The observed outstanding catalytic performance demonstrated by TMCs on the RWGS opened the way for exploring the performance of their two-dimensional (2D) counterparts, the so-called MXenes [22]. First isolated in 2011, these materials have significantly impacted many scientific fields due to their unique properties and composition tunability through surface functionalization and elemental composition [22,23]. MXenes have a general $M_{n+1}X_nT_x$ chemical formula and are generally derived from MAX phases by selective etching of the A element, although layer growth paths have been proposed [24,25]. The M, X, and T_x labels represent an early transition metal, carbon and/or nitrogen, and the surface functionalization (–O, –OH, –H, or –F), respectively, while n = 1–4 represents the thickness of the material measured in number of atomic layers of the X element [26,27]. Regarding surface termination, novel synthetic routes or treatment protocols have shown how to gain unfunctionalized (or bare) MXenes [28–30].

Pristine MXenes have shown excellent CCS capabilities, as confirmed by both molecular simulations and experiments [29,31]. Furthermore, MXenes also feature a high affinity towards H_2, catalyzing its dissociation, often spontaneously, and posing themselves as suitable catalytic materials for hydrogenation reactions [32]. Moreover, CO_2 dissociation into CO + O —usually the reaction limiting step— is feasible on MXenes, requiring overcoming low kinetic energy barriers of up to 0.6 eV [33]. The above outlined possible uses of MXenes as heterogeneous catalysts for CCU technologies are not limited to the RWGS reaction [33]. For instance, partially O-covered Mo_2C MXene has been pointed out as an effective heterogeneous catalyst for the methane dry reforming [34] or for the Fischer–Tropsch Synthesis [9], and even as a support for Cu single atoms in the CO_2 reduction to methanol [35].

Recently, Jurado *et al.* [36] investigated the RWGS as heterogeneously catalyzed by pristine Mo_2C MXene, combining first-principles calculations and microkinetic simulations. While the redox and formate routes were the most plausible pathways for the reaction mechanism, H_2O formation was found to be the rate-limiting step [37], even though optimal CO formation was achieved at ~600 K and low total pressure of 1 bar, in line with subsequent experimental observations on a cleaned Mo_2C MXene, with a peak RWGS performance at *ca.* 700 K and 1 bar [38], hence with capabilities to outperform the industrial benchmark Cu-ZnO-Al_2O_3 catalyst in terms of activity, selectivity, and/or stability.

Although these are promising results, there are aspects of the mechanism of the RWGS reaction catalyzed by Mo_2C that are missing, yet necessary to reach a rational-driven significant advance in conversion optimization. In particular, two main questions remain hitherto unsolved. On the one hand, it has been observed that the CO production during the RWGS is minimal for as-prepared Mo_2CT_x samples; this is, with no treatment of surface functional groups, *e.g.*, –O, whereas the sample treatment at 500 ºC with H_2 —to remove surface –O groups and leave the surface clean— significantly impacts the catalytic performance, raising the CO production by two orders of magnitude, and reaching the performance levels of reference Cu-ZnO-Al_2O_3 catalyst. Thus, the presence/absence of surface –O groups biases the catalytic reaction, but the underlying chemistry is unknown. On the other hand, it is now well known that MXenes, when extracted from a MAX matrix, do not necessarily follow the same ABC layer stacking of the parent MAX phase. There is computational and experimental evidence that, for some MXene compositions, a phase transition towards ABA can be energetically and kinetically prompted [39], also influenced by the termination. Clearly, this may have an impact on the overall surface chemical and catalytic activity [40]. Here, we address these two aspects by performing theoretical calculations based on density functional theory (DFT), combined with microkinetic simulations. These allows us to univocally assess the effect of the O surface termination and of the atomic layer stacking on the RWGS mechanism and catalytic performance on Mo_2C MXene-based catalysts.

2. Computational strategy and models

The RWGS reaction mechanism was investigated over the Mo_2C (0001) MXene pristine and partially O-functionalized surfaces. The basal (0001) plane of the Mo_2C MXene is represented by a $p(3\times3)$ supercell (Fig. 1), large enough to host the reactants, intermediates, and products involved in the RWGS reaction [33,36]. Diverse high-symmetry sites —top, bridge, or hollow sites— were tested for the adsorption of reactants, intermediates, and products regarding different connectivity, orientations, and conformation. Due to the periodic boundary conditions, a vacuum of at least 10 Å along the [0001] direction was included to avoid the interaction between the periodic MXene replicas in this direction.

For the pristine case we focus on the ABA atomic layer stacking (Mo_2C-ABA model) thus complementing a previous study which considered the ABC stacking (Mo_2C-ABC model) [36]. The stability of the ABA-stacked material when compared to the ABC-stacked one is a well-established result from previous studies [39,41,42]. For the partially O-functionalized Mo_2C (*i.e.* $Mo_2CO_{4/3}$ as the two surfaces have a $^2/_3$ O coverage), both ABA ($Mo_2CO_{4/3}$-ABA model) and ABC ($Mo_2CO_{4/3}$-ABC model) atomic layer stackings are considered, see Fig. 1. In the case of –O termination, the –O atoms are located at the three-fold hollow sites, following the same stacking definition as the inner C layer, as this is found to be their optimal position [43]. The O coverage considered involves occupancy of $^2/_3$ of the surface hollows sites as in previous studies [34,35] (*cf.* Fig. 1c). The clustering of pristine sites on the model catalyst surfaces is also justified in terms of stability;

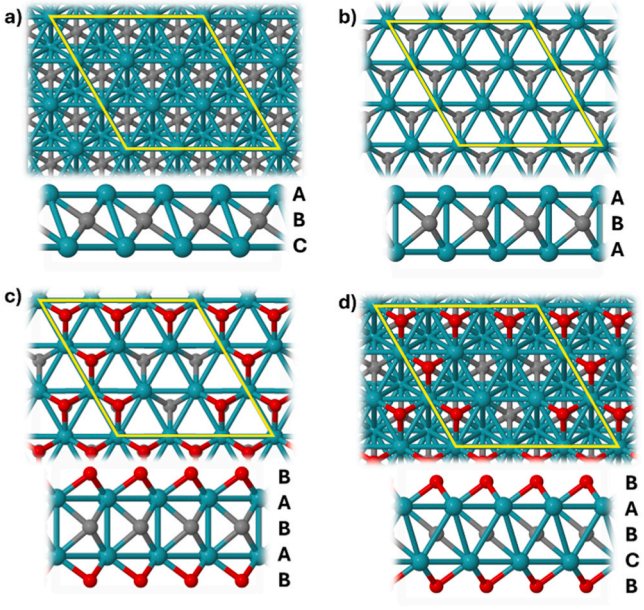

Fig. 1. Top (top) and side (bottom) views of the a) pristine (0001) Mo_2C MXene surface with ABC stacking, b) pristine (0001) Mo_2C MXene surface with ABA stacking, c) partially O-terminated Mo_2C MXene (0001) surface with $^2/_3$ of a monolayer (ML) of –O coverage per surface, with BABAB stacking, and d) partially O-terminated Mo_2C MXene surface model with BABCB stacking. The solid yellow line defines the employed $p(3\times3)$ supercell. C, Mo, and O atoms are depicted by gray, green, and red spheres, respectively.

see discussion in Section S1 and Fig. S1 of the Supporting Information (SI). The presence of oxygen on the surface of the MXene is stable and derived from its synthesis procedure. A cleaning-up procedure requires the H_2 exposure at 700 ºC (*ca.* 1000 K) to remove oxygen as water. This experimental evidence, together with computational studies, reveals that O-free situations are attainable only at very high temperatures and supports the notion that the present $^2/_3$ monolayer (ML) coverage model is reasonable at the evaluated reaction conditions.

The adsorption energy of the *i* species, E^i_{ads}, is defined as;

$$E^i_{ads} = E_{i/MXene} - (E_i + E_{MXene}) + \Delta ZPE, \quad (1)$$

where $E_{i/MXene}$ represents the total energy of species *i* adsorbed on the *p*(3×3) MXene supercell; E_{MXene} is the total energy of the *p*(3×3) MXene supercell depicted in Fig. 1 —either the unfunctionalized Mo_2C-ABA stacking model, or the partially O-functionalized $Mo_2CO_{4/3}$-ABA or $Mo_2CO_{4/3}$-ABC stacked models—, and, finally, E_i stands for the total energy of the isolated *i* species optimized in an asymmetric box of 10×11×12 Å dimensions, carried out at **Γ**-point only. ΔZPE corresponds to the zero-point energy (ZPE) change between the adsorbed and gas phase species. For this term, vibrational frequencies are needed, either for the gas phase molecule or for the adsorbed species, in the latter case disregarding coupling with Mo_2C or $Mo_2CO_{4/3}$ phonons. For the adsorbed species, vibrational modes from frustrated translational and rotational degrees of freedom are accounted for. The diagonalization of the Hessian matrix with elements computed as finite differences of analytical gradients with displacements of 0.015 Å was carried out to obtain such frequencies.

To facilitate a consistent comparison of the present results with those in previous work [36], we followed the very same computational strategy carrying out periodic DFT calculations as implemented in the Vienna *ab initio* simulation package (VASP) [44] and using the same computational setup. Thus, the Perdew-Burke-Ernzerhof (PBE) density functional [45], belonging to the generalized gradient approximation (GGA) family, has been used to account for the exchange and correlation effects. Note that this density functional has shown an excellent performance in describing bulk three-dimensional molybdenum carbide systems [46]. The broadly employed and suited Grimme's D3 approach [47] was used to account for the dispersion interactions [48]. The effect of the core electrons on the valence density was described using the projector augmented wave (PAW) method [49], while a plane-wave basis set with a 415 eV cutoff energy was selected to expand the valence electron density. The numerical integration in the reciprocal space was carried out using a **Γ**-centered 5×5×1 **k**-point grid in the Brillouin zone. Forces below 0.01 eV·Å^{-1} on all atoms and relaxation of the electronic degrees of freedom with a 10^{-6} eV threshold ensure numerical accuracy below 0.04 eV in the geometry optimization calculations, thus close to the chemical accuracy limit [31–33].

Once the minimum energy structures were obtained and characterized, a transition state (TS) search was carried out employing the Dimer method, and minimizing forces acting on atoms below 0.01 eV·Å^{-1} [50]. The frequency analyses were also employed here to confirm the saddle point character of TSs, with only a single imaginary frequency along the reaction path. The activation energy barriers, E_b, of the different reaction steps were obtained as the difference between the ZPE-corrected energies of the TS and of the initial state (IS) configurations. The rate parameters —*i.e.* the equivalent of rate constants in formal kinetics— were obtained from transition state theory as

$$r = \frac{k_B T}{h} \cdot \frac{Q_{TS}}{Q_{IS}} \cdot e^{\left(-\frac{E_b}{k_B T}\right)}, \quad (2)$$

where k_B and *h* are the Boltzmann's and Planck's constants, respectively, while Q_{TS} and Q_{IS} are the partition functions of the TS and IS, respectively. Further details on their expression for the ZPE-corrected E_b can be found in the literature [51]. The desorption rates were estimated assuming late TSs, *i.e.*, $E_b = -E_{ads}$, and a two-dimensional translational and a rotational partition function applied on Q_{TS} [51]. The adsorption rate, r_{ads}, though, was derived from collision theory employing the Hertz-Knudsen equation [52] as;

$$r_{ads} = \frac{A_{site} \cdot p_i \cdot S_i}{\sqrt{2 \cdot \pi \cdot m_i \cdot k_b \cdot T}}, \quad (3)$$

where A_{site} is the area of the adsorption site calculated dividing the supercell area of the MXene surface by the total number of sites in it [53]; p_i corresponds to the partial pressure of the *i* component; S_i corresponds to the sticking coefficient of the *i* component; and m_i is the molecular mass. Here, the sticking coefficient of reactants and products was fixed to unity based on previous estimations of this parameter for these molecules on Pt surfaces (S_i~0.7), on which the adsorbate-adsorbent interactions were of the same order of magnitude [54–56].

The rate parameters described above were used to carry out mean-field microkinetic (MKM) simulations, allowing one to identify the rate-limiting steps of the RWGS reaction for each studied case. All MKM simulations were carried out using the MKMCXX code [57,58], and assuming the quasi-equilibrium approximation. Under these circumstances, one can obtain the surface coverage, θ, for each *i* species and the overall reaction rate. During the catalytic reaction, the adsorption, desorption, and reaction steps are the main occurring processes. Finally, the present MKM simulations neglected the interaction between non-reacting adsorbed species, and they are assumed to be randomly distributed over the derived Mo_2C MXene surface and always available. Such MKM limitations can be overcome with further analysis using kinetic Monte Carlo simulations, including the spatial display of surface chemical moieties and their lateral interactions.

3. Results and discussion

Let us start tackling the stacking —ABA or ABC— effect on relevant properties by comparing adsorption energy differences for reactant —CO_2 and H_2— or product —CO and H_2O— molecules. The results for the bare Mo_2C (0001) surfaces are compiled in Table 1, and show that

Table 1
Relevant energy quantities for the elementary reaction steps of the RWGS reaction on the Mo_2C (0001) surface models with ABA or ABC stacking. The ABC stacking values are taken from Ref. [36]. Activation energy barriers, E_b (in eV) for forward (*fwd*) and backward (*bwd*) reactions, are included together with the reaction energies or energy changes, ΔE (in eV). Note that $\Delta E_{fwd} = -\Delta E_{bwd}$. For completeness, adsorption/desorption steps for CO_2, H_2, CO, and H_2O are included. All provided values provided include the ZPE term.

	Elementary reaction step	Mo_2C-ABC			Mo_2C-ABA		
		E_b		ΔE	E_b		ΔE
		fwd	*bwd*	*fwd*	*fwd*	*bwd*	*fwd*
1	$CO_2^{(g)} + * \rightarrow CO_2*$	—	—	−1.80	—	—	−0.94
2	$H_2^{(g)} + * \rightarrow H_2*$	—	—	−0.92	—	—	−0.62
3	$CO* \rightarrow CO^{(g)} + *$	—	—	2.39	—	—	1.83
4	$H_2O* \rightarrow H_2O^{(g)} + *$	—	—	0.95	—	—	0.63
5	$H_2* + * \rightarrow 2H*$	0.01	0.93	−0.92	0.13	1.08	−0.95
6	$CO_2* + * \rightarrow CO* + O*$	0.47	1.90	−1.43	0.03	1.44	−1.41
7	$O* + H* \rightarrow OH* + *$	1.59	0.70	0.88	1.27	0.47	0.81
8	$OH* + H* \rightarrow H_2O* + *$	1.68	0.32	1.36	1.84	0.41	1.43
9	$CO_2* + H* \rightarrow HCOO* + *$	0.56	0.48	0.08	0.73	0.29	0.44
10	$HCOO* + * \rightarrow HCO* + O*$	0.29	1.30	−1.00	~0	1.80	−1.80
11	$HCO* + * \rightarrow H* + CO*$	0.36	0.86	−0.50	0.63	1.66	−1.03
12	$CO_2* + H* \rightarrow$ *trans*-COOH* + *	0.84	0.01	0.83	1.16	0.69	0.46
13	*trans*-COOH* → *cis*-COOH*	0.27	0.34	−0.07	0.22	0.33	−0.11
14	*cis*-COOH* + * → COH* + O*	0.49	1.30	−0.81	0.48	1.62	−1.14
15	$COH* + * \rightarrow CO* + H*$	0.62	1.43	−0.81	0.63	1.66	−1.03

CO_2 molecule adsorption is exothermic by −1.80 or −0.94 eV for ABC or ABA stacking, respectively, displaying a geometry consistent with the so-called activated CO_2. For the ABA stacking, the calculated C-O bond lengths of adsorbed CO_2 are 1.34 and 1.25 Å, elongated as previously reported for the ABC stacking with values of 1.51 and 1.26 Å [31]. On the ABC (ABA) surface, H_2 adsorbs molecularly with an adsorption energy of −0.92 (-0.62 eV) and an elongated molecular bond of 0.89 Å (0.85 Å), compared to the value of 0.75 Å in the gas phase, and thus in line with a Kubas adsorption mode [59,60]. Concerning the products, CO features the largest E_{ads} with values of −2.39 and −1.83 eV for Mo_2C with ABC and ABA stacking, respectively. Finally, the H_2O molecule interacts weakly, with E_{ads} values of −0.95 and −0.63 eV. All in all, the results clearly show that the Mo_2C (0001)-ABC surface model has a higher chemical activity compared to Mo_2C-ABA, with enhanced adsorption energies by 0.30–0.86 eV, in concordance with Mo_2C-ABC being less stable than Mo_2C-ABA [39], and therefore, more prone to adsorb species upon to compensate its inherent instability, as observed previously on TMC surfaces [61]. From *Le Sabatier* principle, the ABA stacking would be a better catalyst for the RWGS, adsorbing species in a more moderate fashion.

Regarding partially O-covered models ($Mo_2CO_{4/3}$), the reactants adsorb much more weakly than on the bare Mo_2C models, as shown in Table 2. In particular, when going from the bare Mo_2C to the partially O-covered $Mo_2CO_{4/3}$ surface, the CO_2 adsorption energies for $Mo_2CO_{4/3}$-ABC ($Mo_2CO_{4/3}$-ABA) change from –1.80 (–0.94) to –0.18 (–0.31) eV. This implies that, in the presence of the O surface termination, the ABA-stacked MXene becomes the most active towards CO_2 adsorption, although by a small margin. In turn, H_2 adsorption energies on partially O-covered Mo_2C, –0.07 (–0.06) eV, are around a tenth of the ones calculated for the bare ABC (ABA) surface and do not change with the atomic layer stacking of the material. Concerning the reaction products, H_2O adsorption strength does not change much with either the O coverage or the stacking, as its adsorption energy on ABC (ABA) partially O-covered surface are –0.75 (–0.73) eV, which are similar to the ones found for bare Mo_2C. In these three cases —CO_2, H_2, and H_2O— stacking has nearly no effect, given they are essentially physisorbed, which are known to be surface-insensitive. The exception is CO, which remains quite strongly adsorbed in the vicinity of the O surface groups, changing from –2.11 eV on Mo_2C on average to –1.80 (–1.23) eV on the $Mo_2CO_{4/3}$-ABC ($Mo_2CO_{4/3}$-ABA). This again poses the more stable ABA stacking as the less active surface, as for pristine Mo_2C models. Overall, the activation of CO and CO_2 molecules is significantly more exothermic on bare Mo_2C supports, while the activation of H_2O and CO is more exothermic on $Mo_2CO_{4/3}$, regardless of the stacking. These differences in the adsorption of reactants and products have an impact on the catalyst production, as will be discussed below with reference to the results of the microkinetic modelling.

Table 2
Relevant energy quantities for the elementary reaction steps of the RWGS reaction on the $Mo_2CO_{4/3}$(0001) surface models with ABC or ABA stacking. Activation energy barriers, E_b (in eV) for forward (*fwd*) and backward (*bwd*) reactions, are included together with the reaction energies or energy changes, ΔE (in eV). Note that $\Delta E_{fwd} = -\Delta E_{bwd}$. For completeness, adsorption/desorption steps for CO_2, H_2, CO, and H_2O are included. All provided values provided include the ZPE term.

	Elementary reaction step	$Mo_2CO_{4/3}$ (ABC)			$Mo_2CO_{4/3}$ (ABA)		
		E_b		ΔE	E_b		ΔE
		fwd	*bwd*	*fwd*	*fwd*	*bwd*	*fwd*
1	$CO_2^{(g)} + * \rightarrow CO_2*$	—	—	−0.34	—	—	−0.31
2	$H_2^{(g)} + * \rightarrow H_2*$	—	—	−0.07	—	—	−0.06
3	$CO* \rightarrow CO^{(g)} + *$	—	—	1.80	—	—	1.23
4	$H_2O* \rightarrow H_2O^{(g)} + *$	—	—	0.75	—	—	0.73
5	$H_2* + * \rightarrow 2H*$	0.03	1.41	−1.38	0.01	1.50	−1.49
6	$CO_2* + * \rightarrow CO* + O*$	0.01	0.27	−0.26	0.01	0.29	−0.28
7	$O* + H* \rightarrow OH* + *$	1.41	0.91	0.50	1.49	0.91	0.58
8	$OH* + H* \rightarrow H_2O* + *$	1.05	0.47	0.58	2.16	0.29	1.87

These activity trends are generally kept when drawing the reaction energy profiles. Here, the existence of two well-defined reaction routes [36] is worth highlighting: The so-called redox mechanism, where CO_2 adsorbs and dissociates into CO* + O* —* denoting a surface site—, and O* gets hydrogenated leading to H_2O, see Fig. 2, and the associative mechanism, where CO_2 gets hydrogenated first. Regarding the associative mechanism, two sub-routes depend on whether the C atom or the O atom of CO_2 gets hydrogenated first, leading to formate (HCOO*) or carboxyl (COOH*) intermediates, respectively. As shown in Fig. 2, formate can dissociate into HCO* and O*, and the resulting HCO* species subsequently dissociates into H* and CO*, thus leading to an alternative formate-mediated CO_2* dissociation. In the case of carboxyl, usually, two isomers may exist on the surface, the *trans*- and *cis*-COOH*, which can dissociate into CO* + OH*. This route avoids forming O* at any stage, as the OH* can be hydrogenated towards H_2O*, see Fig. 2.

The three RWGS reaction routes were thus investigated on the bare Mo_2C-ABC and Mo_2C-ABA models, while on partially O-covered $Mo_2CO_{4/3}$-ABA and $Mo_2CO_{4/3}$-ABC, only the redox mechanism was considered; explained in detail below. Previous works [33,34,38] have shown that bare MXenes excel at dissociating chemical species into individual atoms, whereas, concomitantly, they have a hard time carrying out the reverse process. The RWGS involves bond-breaking in the early stages and bond-formation in the later ones. Therefore, one should expect the adsorption and dissociation steps to be thermodynamically and kinetically driven and the desorption and associative steps less keen to occur. As the calculations show, CO_2 dissociation will likely proceed without prior hydrogenation. In contrast, the hydrogenation of the resulting O* is likely energy-demanding, hinting that the RWGS redox route is most favorable.

The reaction energy profiles of RWGS *via* the redox mechanism on the four Mo_2C MXene surfaces considered here are shown in Fig. 3 and confirm the above predictions. As can be seen, the calculated CO_2

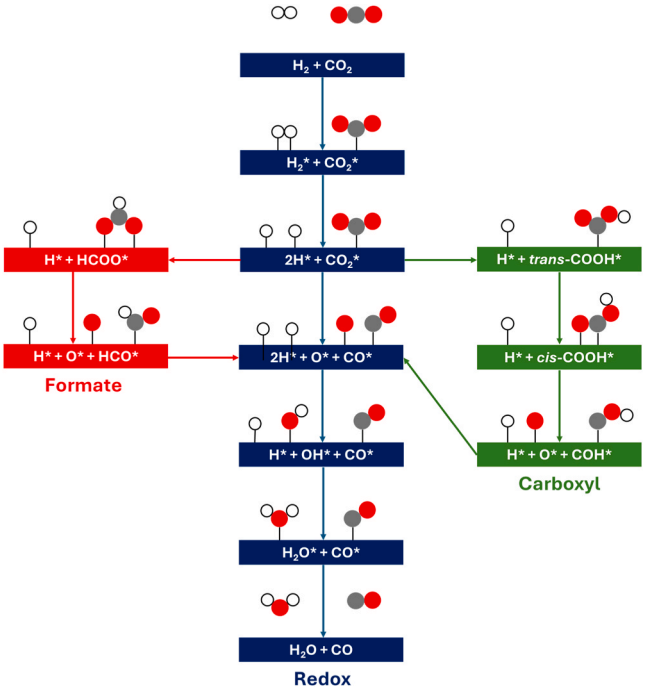

Fig. 2. Schematic view of the RWGS mechanism, including redox, formate, and carboxyl routes depicted by black, red, and green lines, respectively. The rectangles represent the surface, and the circles represent atoms of hydrogen (white), carbon (grey), or oxygen (red). Adsorbed situations are marked with a surface-active site, *.

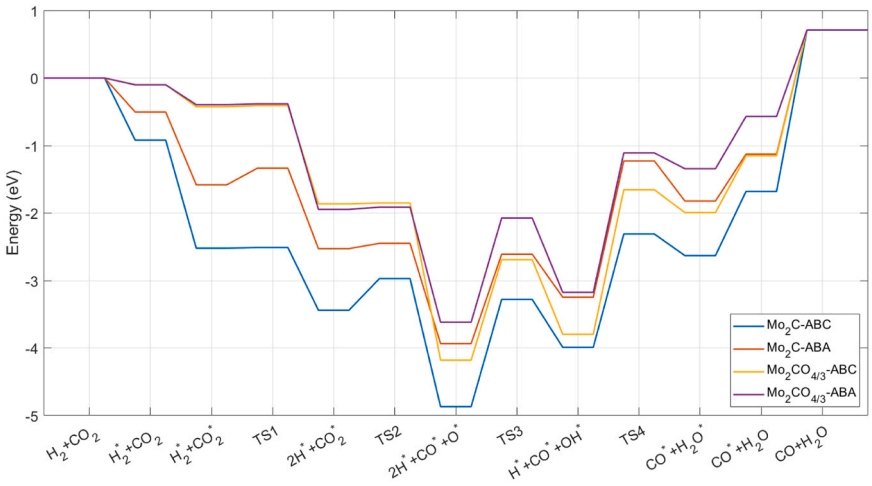

Fig. 3. RWGS reaction energy profile —including ZPE— *via* the redox mechanism, as catalyzed by pristine yet differently stacked Mo_2C-ABA and Mo_2C-ABC (0001), and partially O-terminated Mo_2C (0001) surfaces, $Mo_2CO_{4/3}$-ABA or $Mo_2CO_{4/3}$-ABC. TS1, TS2, TS3, and TS4 denote the TSs of steps **5-8** of Tables 1 and 2.

dissociation energy barriers on Mo_2C-ABA and partially O-covered $Mo_2CO_{4/3}$-ABA and $Mo_2CO_{4/3}$-ABC, with transition state denoted TS2 in Fig. 3, are indeed negligible, of at most 0.03 eV as gathered in Tables 1 and 2. This contrasts with the same barrier on Mo_2C-ABC (0.47 eV). Reaction energy plots in Fig. 3 hint that, from the four surfaces shown, the partially O-covered $Mo_2CO_{4/3}$-ABA would be the most suited for catalyzing the RWGS through the redox path, with very low H_2 and CO_2 dissociation barriers while featuring the most moderate reaction exothermicity and adsorption energies. In contrast, the other RWGS routes on Mo_2C-ABC and Mo_2C-ABA involve energy barriers around 0.7 eV or more (*cf.* Table 1) to form the intermediate species between the CO_2* and CO*+O* stages. Energy barriers around 0.7 eV are not prohibitive, but the nearly spontaneous CO_2 dissociation on all surfaces except Mo_2C-ABC is more favored. The reaction energy profiles for the formate and carboxyl routes are given in Figs. S2 and S3 of the SI. In turn, H_2 dissociates practically spontaneously upon adsorption on all four surfaces studied (*cf.* Tables 1 and 2), showing that H_2 will be prone to better interact and dissociate on pristine MXene sites rather than on Mo-O sites on the O-covered models.

Still, the above reaction energy profiles and discussion only hint at the reaction kinetics. To better assess the reaction kinetics, a series of MKM simulations have been carried out. MKM aims to analyze the influence of working conditions —temperature, T, and gases partial pressures, p_i— on the catalyst production, here seized by the turnover frequency, TOF. The numerical integration is carried out subject to initial conditions from time $t = 0$ s until steady state, *i.e.*, the surface coverages no longer changing with time. To facilitate the comparison with previous studies [36], a H_2:CO_2 ratio of 2:1 is selected, also supported by available experimental data [62,63]. In the MKM simulations, all available elementary reaction steps —from redox, carboxyl, and formate routes— are considered, as compiled in Table 1, including forward (*fwd*) and backward (*bwd*) activation energy barriers, E_b, and the reaction energy changes, ΔE, for pristine Mo_2C MXenes with ABA and ABC stackings, while equivalent partially O-covered values are shown and discussed below.

Attention is driven first to the coverage evolution of the different reaction species as a function of T, see Fig. 4. At first sight, the RGWS reaction on Mo_2C-ABC involves more intermediates in the temperature range of 300–650 K when compared to Mo_2C-ABA which is relatively less complex. At a very low temperature of 300 K, the Mo_2C-ABC model is mainly covered by H adatoms resulting from H_2* dissociation. Any adsorbed CO_2 becomes hydrogenated to form HCOO*, which is, in principle, prompted by the high H* coverage. On Mo_2C-ABA, though, despite the high H* coverage, one would expect less HCOO*; since E_b for Mo_2C-ABC is 0.56 eV, whereas it is 0.73 eV for Mo_2C-ABA. However,

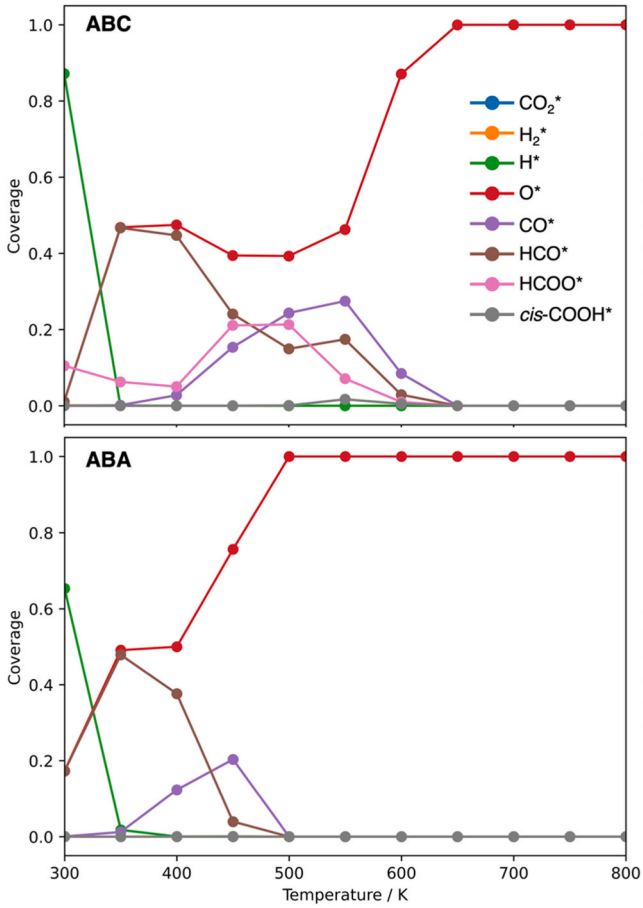

Fig. 4. Surface coverage evolution with T for the RGWS reaction on the Mo_2C (0001) surface with ABC (top) and ABA (bottom) stacking. Coverages were taken with input H_2:CO_2 2:1 ratio and a total pressure of 1 bar. The results concerning the ABC-stacked surface were taken from Ref. [36].

equal parts of HCO* and O* are found, in line with the very easy HCOO* decomposition on the Mo_2C-ABA model, with an E_b below 0.01 eV, compared to the 0.29 eV barrier on Mo_2C-ABC.

On both models, above $T = 350$ K, H* vanishes, either consumed in any reaction mechanism or backreacted towards H_2* and desorbed. Also, the CO_2* + H*→HCOO*→HCO* + O* sequence of elementary

steps seems to be followed, with a certain existence of HCOO* on Mo_2C-ABC, in principle due to an easier formation of this species, either from the forward (CO_2* + H*) or backward (HCO* + O*) reactions when compared to Mo_2C-ABA. At $T > 400$ K, the redox route opens, as observed by an excess of O* with respect to HCO* and the appearance of CO* by essentially equal amounts. By raising the temperature, the redox route gains relevance on both Mo_2C-ABC and Mo_2C-ABA models, while formate loses the leadership, even if HCOO* presence is kept on the Mo_2C-ABC model. The main difference is the peak of CO* presence, achieved at 450 K for Mo_2C-ABA and 550 K for Mo_2C-ABC. From such temperatures, a saturation of O* is achieved on both models, at 500 K for Mo_2C-ABA and 650 K for Mo_2C-ABC. Altogether, there is a parallelism of ABA and ABC kinetics in *i*) the low-temperature preference for formate associative mechanism, *ii*) the opening of redox mechanism at 400 K, and *iii*) the main relevance at temperatures above 400 K, until *iv*) a critical temperature at which the Mo_2C surface becomes fully occupied by O atoms. However, it is worth noting that the reactive stages on Mo_2C-ABA are found at temperatures ~100 K lower than on Mo_2C-ABC.

The above discussion relates only to surface species, and the formation of $CO^{(g)}$ and $H_2O^{(g)}$ products needs also to be assessed. This is tackled in Fig. 5 reporting turnover frequencies (TOFs) heating contour maps of $CO^{(g)}$ production using H_2:CO_2 ratio of 2:1 on Mo_2C-ABC and Mo_2C-ABA models. For completeness $H_2O^{(g)}$ production is depicted in Figs. S4 and S5 of the SI. The ABC stacking features the largest CO production in the 550–620 K temperature range, highlighted in Fig. 5 by yellow stripe, with a peak of $3.37{\cdot}10^{-3}$ molecules·site^{-1}·s^{-1} at 1 bar of total pressure [36]. At this temperature and pressure, the ABA stacking performance is seven orders of magnitude lower, $2.53{\cdot}10^{-10}$ molecules·site^{-1}·s^{-1}, and higher temperatures of ~800 K are required to achieve a comparable (or even greater) $CO^{(g)}$ production. In fact, a much higher TOF, of about 0.41 molecules·site^{-1}·s^{-1}, is achieved on Mo_2C-ABA at 1 bar and 850 K, while at the same conditions, Mo_2C-ABC performs worse with a TOF of $3.26{\cdot}10^{-6}$ molecules·site^{-1}·s^{-1}. On the Mo_2C-ABA model, the performance slightly increases with total pressure, to 3.47 molecules·site^{-1}·s^{-1} at 850 K and 10 bar (further details in Tables S1 and S2). Note that the TOF achieved at 500 K and 7 bar is found to be a numerical artefact derived from the microkinetic analysis. The highest performances of either Mo_2C-ABC or Mo_2C-ABA at temperatures around 600 or 800 K, respectively, are in line with the experimental highest peak at *ca.* 700 K [38], knowing that mean-field MKM simulations can deviate peak performances by ± 100 K [64].

We now drive the discussion to the impact of having a partial O-termination on the examined MXene models. This is spurred by the experimental key performance also previously suggested using theory [34] for $^2/_3$ ML of surface –O groups [34,38] at each surface, by the O-affinity of both Mo_2C-ABA and Mo_2C-ABC surface models at high temperatures, and by the present observation of the peak performance when having a partial O* coverage as observed on pristine ABC, see Figs. 4 and 5. Note here in passing that the stacking notation for $Mo_2CO_{4/3}$-ABA and $Mo_2CO_{4/3}$-ABC models is BABAB and BABCB, respectively, see Fig. 1. As observed in Fig. 6 for $CO^{(g)}$ production, and on Figs. S6 and S7 of the SI for H_2O(g) production, in general terms, the activity of the $Mo_2CO_{4/3}$ (0001) surface models get reduced when having such an O* coverage, as above commented, also reducing the difference between stackings, with only CO featuring a markedly stronger bonding on $Mo_2CO_{4/3}$-ABC.

As commented above, the essentially barrierless CO_2* dissociation step, either for $Mo_2CO_{4/3}$-ABC or $Mo_2CO_{4/3}$-ABA, prompts the reaction to follow the redox path, with kinetic and thermodynamic values are compiled in Table 2. In addition to CO_2* dissociation, H_2* dissociation is also favored with a $^2/_3$ of a ML of –O groups, with E_b values being also essentially barrierless. Thus, again, OH* and H_2O* formations could be rate-determining steps (RDS) for $Mo_2CO_{4/3}$-ABC and $Mo_2CO_{4/3}$-ABA, respectively, with E_b values of 1.41 and 2.16 eV. Actually, as seen in Table 1, H_2O* formation was already the RDS on pristine Mo_2C-ABC and Mo_2C-ABA models, with E_b values of 1.68 and 1.84 eV, respectively.

Thus, based on the TOF color maps in Figs. 5 and 6, one would expect the RWGS to be slightly favored on $Mo_2CO_{4/3}$-ABC compared to the pristine case while disfavored on $Mo_2CO_{4/3}$-ABA. As observed, the better assessment of kinetics by MKM simulations, in Fig. 6 —equivalent Figs. S7 and S8 of the SI for $H_2O^{(g)}$ production— reveal that the performance is similar for low temperatures, up to *ca.* 650 K on $Mo_2CO_{4/3}$-ABC and $Mo_2CO_{4/3}$-ABA models. From this temperature on, the RWGS performance increases for both models, but especially for the ABC one, reaching TOFs three orders of magnitude higher than on $Mo_2CO_{4/3}$-ABA at a temperature of *ca.* 800 K. Curiously, on $Mo_2CO_{4/3}$, the high-temperature performance is better achieved on ABC (*cf.* Fig. 6), while the opposite is found on the pristine Mo_2C models (*cf.* Fig. 5).

Additional sensitive analysis of the microkinetic simulations is performed to quantify the uncertainties of the DFT calculations and quantify the effect on the catalytic production. Thus, we focus on the $Mo_2CO_{4/3}$ MXene with ABC stacking at 850 K and 1 bar. At these conditions, the partially O-covered MXene shows the largest TOF values (*ca.* 112 molecules·site^{-1}·s^{-1}, see Table S2 of the SI). To further validate this conclusion, we varied different kinetic and thermodynamic parameters one by one taking as reference our initial microkinetic simulations: First, the TOF was found to sensibly decrease to 17.7 molecules·site^{-1}·s^{-1} when increasing only the CO_2 dissociation energy barrier by 0.2 eV, in line with typical DFT accuracy. Note, however, that this elementary reaction is here predicted to be barrierless, see Table 2). On the other

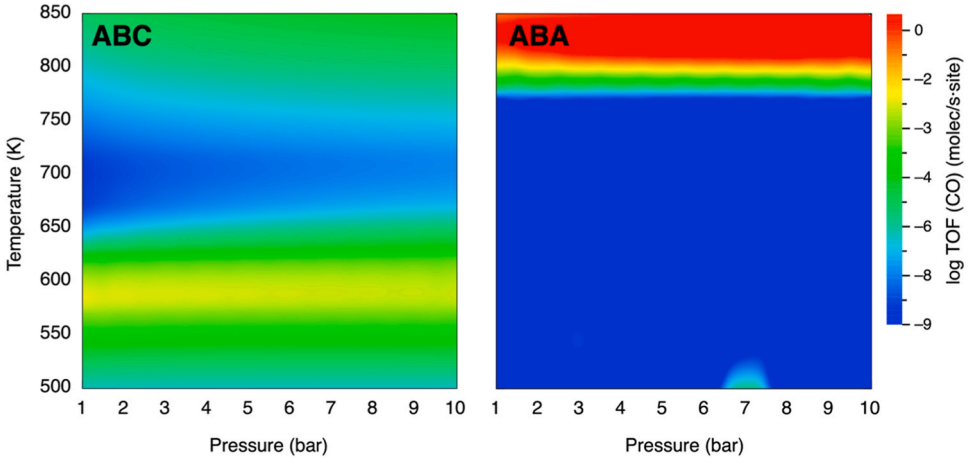

Fig. 5. Color map of TOF under different *p* and *T* conditions for the RGWS reaction on the Mo_2C (0001) surface with ABC (left) and ABA (right) stacking for the $CO^{(g)}$ production. The TOF scale corresponds to the logarithm with base 10. The results concerning the ABC-stacked surface were taken from Ref. [36].

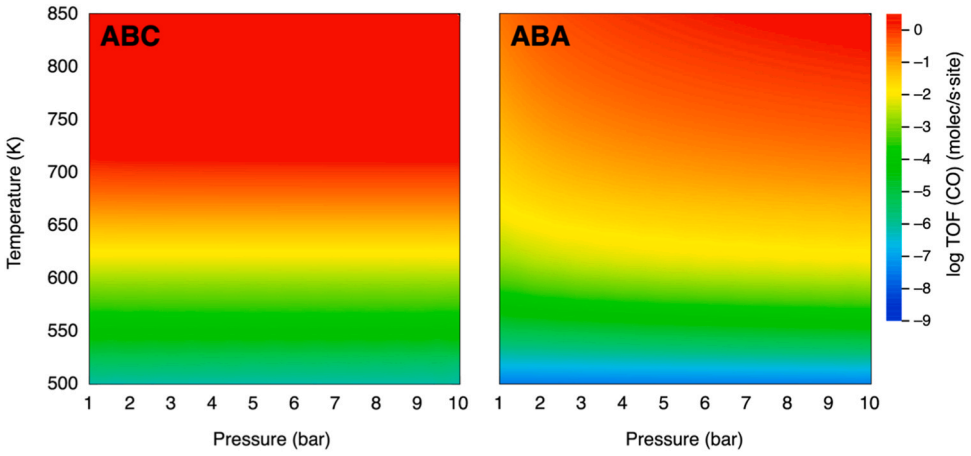

Fig. 6. Color map of TOF under different *p* and *T* conditions for the RGWS reaction on the (0001) $Mo_2CO_{4/3}$ MXene surface models with ABC (left) and ABA (right) stacking for the CO production. The TOF scale corresponds to the common logarithm with base 10.

hand, the TOF production significantly increases up to *ca.* 542 molecules·site^{-1}·s^{-1} when increasing the CO_2 adsorption energy also by just 0.2 eV. Furthermore, a CO desorption energy drop of 0.2 eV (*ca.* 1.60 eV) just slightly increases the TOF up to nearly 210 molecules·site^{-1}·s^{-1}. Finally, artificially decreasing the energy barriers of limiting steps of OH and H_2O formation by 0.2 eV results into negligible variations in the TOF. Such effects are likely translated to the other MXene models, given the similarities in the elementary steps and mechanisms. Thus, from this analysis, it arises the combination of low dissociative energy for the CO_2 molecule and a high exothermic CO_2 interaction, plus an easy CO desorption, are key steps in optimizing the RWGS process.

At this stage, it is worth correlating the obtained TOFs with those from the experiments [38]. There, it was found that a $CO_{(g)}$ production of about 1500 mg CO h^{-1} g$_{cat}^{-1}$ when departing from H_2-treated, pristine 2D-Mo_2C and performing the RWGS at 430 °C (703.15 K). Even if the H_2:CO mixture employed was 3:1 and here 2:1, one can estimate the log TOF of CO, assuming that all the Mo_2C is exposed (even if in the experiments only a part is expose), and that there are two surface active sites per Mo_2C sheet, and that an active site is comprised within the employed $p(3\times3)$ cell. Considering this, a rough estimate for the experimental log TOF is −1.86, while the present MKM simulations for pristine Mo_2C-ABC and Mo_2C-ABA at these conditions are −8.46 and −12.76, respectively. This indicates that the pristine surfaces are far from being adequate catalysts and also that the corresponding theoretical models do not perform well. However, the results for the models with $^2/_3$ ML –O coverage are much closer to the experiment. In particular, the log TOF of $Mo_2CO_{4/3}$-ABA of −1.56 is the closest to the experimental value, especially when compared to the $Mo_2CO_{4/3}$-ABC estimate of −0.12 or the pristine values above, with differences between theory and experiment raising from *e.g.* the mean-field microkinetic modeling approach, of mass-transport limitations in experiments, here not accounted for. Still, this better agreement of $Mo_2CO_{4/3}$ (0001)-ABA model reconciles theory forecasts with experiments, in that *i*) ABA is known to be energetically preferred over ABC for the Mo_2C MXene, especially when O-covered [39], *ii*) the observed better catalytic performance of partially O-covered Mo_2C [35,38], and *iii*) the need of H_2-pretreatment of Mo_2C to remove surface terminations, even if under operando conditions the catalyst gets partially O-covered [38,64]. Further, the MKM simulations show that the catalyst could benefit from an increased performance by a few orders of magnitude when the Mo_2C MXene could be kept in its ABC stacking, leaving this door open for future catalyst engineering.

4. Conclusions

The present first-principles DFT calculations combined with microkinetic MKM simulations on the RWGS reaction over the (0001) molybdenum carbide MXene surface unfolded the influence of the MXene stacking and the partial –O termination over the resulting CO gas production. The results show that CO gas production can occur at mild reaction conditions of pressure, gas mixture, and temperature, where the formation and release of water is the limiting step. The pristine Mo_2C MXene models feature higher chemical activity than the partially O-terminated counterparts, especially when the reaction occurs on the less stable ABC stacking, prompting the rapid dissociation of reactants but also the more costly product formation.

Based on MKM simulations, pristine Mo_2C-ABA MXene leads to higher TOF values than its ABC counterpart at a temperature above 800 K, while ABC stacking promotes higher production than the ABA one at 600 K. Even if the associative mechanism is followed at low temperatures, the redox path is the main reaction route at higher temperatures on any Mo_2C stacking. This leads to the catalyst being covered by O adatoms.

The partial –O coverage significantly increases the CO gas production following the redox mechanism on the $Mo_2CO_{4/3}$-ABC model, surpassing the performance of the $Mo_2CO_{4/3}$-ABA one, however, the latest is a priori more stable and closer to the reported experimental TOF. Therefore, this study suggests that the catalytic performance of the molybdenum carbide MXene for the reverse water gas shift reaction can be increased by guiding its synthesis to favor the ABC stacking and a partial termination of its surface with oxygen atoms. Possibly most importantly, a key message of this work is that the atomic layer stacking and surface termination of a MXene must not be ignored when computationally studying catalysis on MXenes to realistically tackle experimental reactions.

Author contributions

The manuscript was written with contributions from all authors. All authors have approved the final version of the manuscript.

CRediT authorship contribution statement

José D. Gouveia: Writing – review & editing, Writing – original draft, Visualization, Methodology, Investigation, Formal analysis, Data curation. **Ángel Morales-García:** Writing – review & editing, Writing – original draft, Visualization, Methodology, Investigation, Formal analysis, Data curation. **Francesc Illas:** Writing – review & editing, Validation, Software, Resources, Funding acquisition, Formal analysis. **José**

R. B. Gomes: Writing – review & editing, Validation, Supervision, Software, Resources, Investigation, Funding acquisition, Formal analysis. **Francesc Viñes:** Writing – review & editing, Writing – original draft, Visualization, Validation, Supervision, Software, Resources, Project administration, Methodology, Investigation, Funding acquisition, Formal analysis, Conceptualization. **Aleix Comas-Vives:** Writing – review & editing, Validation, Supervision, Software, Resources, Project administration, Investigation, Funding acquisition, Formal analysis. **Anna Vidal López:** Writing – review & editing, Methodology, Investigation, Formal analysis, Data curation.

Declaration of Competing Interest

The authors declare that they have no known competing financial interests or personal relationships that could have appeared to influence the work reported in this paper.

Acknowledgements

The authors thank the Spanish *Ministerio de Ciencia e Innovación* (MCIN) and *Agencia Estatal de Investigación* (AEI) MCIN/AEI/10.13039/501100011033 for PID2020–115293RJ-I00, PID2021–126076NB-I00, PID2021–128416NB-I00, and TED2021–129506B-C22 projects, funded partially by FEDER *Una manera de hacer Europa*, the pre-doctoral grant to AVL (PRE 2019–089647) as well as for the *Unidad de Excelencia María de Maeztu* CEX2021–001202-M granted to the IQTCUB. Generalitat de Catalunya funding is also acknowledged through 2021SGR00079 grants. This work was also financed by projects CICECO-Aveiro Institute of Materials, with refs. UIDB/50011/2020, UIDP/50011/2020 and LA/P/0006/2020, ForTheShift, with ref. 2022.02949.PTDC, and project Ref. 2022.15802.CPCA.A2, with funds from FCT/MEC (PIDDAC). JDG thanks the Portuguese Foundation for Science and Technology (FCT) through the grants with Refs. 2022.00719.CEECIND and 2023.06511.CEECIND, in the scope of the Individual Calls to Scientific Employment Stimulus – 5th and 6th Editions. FV thanks the ICREA Academia Award 2023 Ref. Ac2216561. Finally, the COST Action CA18234 is greatly acknowledged.

Appendix A. Supporting information

Supplementary data associated with this article can be found in the online version at doi:10.1016/j.mtcata.2024.100076.

References

[1] L.J.R. Nunes, The rising threat of atmospheric CO_2: A review on the causes, impacts, and mitigation strategies, Nanomaterials 10 (66) (2023) 1–22, https://doi.org/10.3390/environments10040066.
[2] J. Hansen, M. Sato, R. Ruedy, K. Lo, D.W. Lea, M. Medina-Elizade, Global temperatura change. Proc. Natl. Acad. Sci. USA 103 (2006) 14288–14293, https://doi.org/10.1073/pnas.0606291103.
[3] K.J. Kroeker, R.L. Kordas, R. Crim, I.E. Hendriks, L. Ramajo, G.S. Singh, C. M. Duarte, J.-P. Gattuso, Impacts of ocean acidification on marine organisms: Quantifying sensitivities and interaction with warming, Glob. Change Biol. 19 (2013) 1884–1896, https://doi.org/10.1111/gcb.12179.
[4] I. Ghiat, T. Al-Ansari, A review of carbon capture and utilization as a CO_2 abatement opportunity within the EWF nexus., 101432, J. CO_2 Util. 45 (2021) 1–14, https://doi.org/10.1016/j.jcou.2020.101432.
[5] F.A. Rahman, M.M. Aziz, R. Saidur, W.A. Bakar, M.R. Hainin, R. Putrajaya, N. A. Hassan, Pollution to solution: Capture and sequestration of carbon dioxide (CO_2) and its utilization as a renewable energy source for a sustainable future, Renew. Sust. Energ. Rev. 71 (2017) 112–126, https://doi.org/10.1016/j.rser.2017.01.011.
[6] R.A. Sheldan, Fundamentals of green chemistry: Efficiency in reaction design, Chem. Soc. Rev. 41 (2012) 1437–1451, https://doi.org/10.1039/C1CS15219J.
[7] Á. Morales-García, F. Viñes, J.R.B. Gomes, F. Illas, Concepts, models, and methods in computational heterogeneous catalysis illustrated through CO_2 conversion, WIREs Comput. Mol. Sci. 11 (2021) e1530, https://doi.org/10.1002/wcms.1530.
[8] U. Guharoy, T.R. Reina, S. Gu, Q. Cai, Mechanistic insights into selective CO_2 conversion via RWGS on transition metal phosphides: A DFT study, J. Phys. Chem. C. 123 (2019) 22918–22931, https://doi.org/10.1021/acs.jpcc.9b04122.
[9] H. Jahangiri, J. Bennett, P. Mahjoubi, K. Wilson, S. Gu, A review of advanced catalyst development for Fischer-Tropsch synthesis of hydrocarbons from biomass derived syn-gas, Catal. Sci. Technol. 4 (2014) 2210–2229, https://doi.org/10.1039/C4CY00327F.
[10] E. Kountoupi, A.J. Barrios, Z. Chen, C.R. Müller, V.V. Ordomsky, A. Comas-Vives, A. Fedorov, The Impact of Oxygen Surface Coverage and Carbidic Carbon on the Activity and Selectivity of Two-Dimensional Molybdenum Carbide (2D-Mo_2C) in Fischer–Tropsch Synthesis, ACS Catal. 14 (2024) 1834–1845, https://doi.org/10.1021/acscatal.3c03956.
[11] J.L.C. Fajín, M.N.D.S. Cordeiro, J.R.B. Gomes, Fischer-Tropsch Synthesis on Multicomponent Catalysts: What Can We Learn from Computer Simulations? Catalysts 5 (2015) 3–17, https://doi.org/10.3390/catal5010003.
[12] G. Zhou, F. Xie, L. Deng, G. Zhang, H. Xie, Supported mesoporous Cu/$CeO_{2-\delta}$ catalyst for CO_2 reverse water-gas shift reaction to syngas, Int. H. Hydrog. Energy 45 (2020) 11380–11393, https://doi.org/10.1016/j.ijhydene.2020.02.058.
[13] D. Kobayashi, H. Kobayashi, K. Kusada, T. Yamamoto, T. Toriyama, S. Matsumura, S. Kawaguchi, Y. Kubota, M. Haneda, S.M. Aspera, H. Nakanishi, S. Arai, H. Kitagawa, Boosting reverse water-gas shift reaction activity of Pt nanoparticles through light doping of W, J. Mater. Chem. A 9 (2021) 15613–15617, https://doi.org/10.1039/D1TA03480D.
[14] M. Zhou, Q. Ge, X. Zhu, Catalytic reduction of CO_2 to CO via reverse water gas shift reaction: Recent advances in the design of active and selective supported metal catalysts, Trans. Tianjin Univ. 26 (2020) 172–187, https://doi.org/10.1007/s12209-020-00246-8.
[15] R. Tang, Z. Zhu, C. Li, M. Xiao, Z. Wu, D. Zhang, C. Zhang, Y. Xiao, M. Chu, A. Genest, G. Rupprechter, L. Zhang, X. Zhang, L. He, Ru-catalyzed reverse water gas shift reaction with near-unity selectivity and superior stability, ACS Mater. Lett. 3 (2021) 1652–1659, https://doi.org/10.1021/acsmaterialslett.1c00523.
[16] L. Chen, R.R. Unocic, A.S. Hoffman, J. Hong, A.H. Braga, Z. Bao, S.R. Bare, J. Szanyi, Unlocking the catalytic potential of TiO_2-Supported Pt aingle Atoms for the reverse water–gas shift reaction by altering their chemical environment, JACS Au 1 (2021) 977–986, https://doi.org/10.1021/jacsau.1c00111.
[17] S.-I. Fujita, M. Usui, N. Takezawa, Mechanism of the reverse water gas shift reaction over Cu/ZnO catalyst, J. Catal. 134 (1992) 220–225, https://doi.org/10.1016/0021-9517(92)90223-5.
[18] R.B. Levy, M. Bodart, Platinum-like behaviour of tungsten carbide in surface catalysis, Science 181 (1973) 547–549, https://doi.org/10.1126/science.181.4099.547.
[19] Z. Lin, S.R. Denny, J.G. Chen, Transition metal carbides and nitrides as catalysts for thermochemical reactions, J. Catal. 404 (2021) 929–942, https://doi.org/10.1016/j.cat.2021.06.022.
[20] A. Pajares, H. Prats, A. Romero, F. Viñes, P.Ramírez de la Piscina, R. Sayós, N. Homs, F. Illas, Critical effect of carbon vacancies on the reverse water gas shift reaction over vanadium carbide catalysts, Appl. Catal. B: Environ. 267 (2020) 118719, https://doi.org/10.1016/j.apcatb.2020.118719.
[21] H. Jing, Q. Li, J. Wang, D. Liu, K. Wu, Theoretical study of the reverse water gas shift reaction on Copper modified β-Mo_2C(001) surfaces, J. Phys. Chem. C. 123 (2019) 1235–1251, https://doi.org/10.1021/acs.jpcc.8b09884.
[22] M. Naguib, M. Kurtoglu, V. Presser, J. Lu, J. Niu, M. Heon, L. Hultman, Y. Gogotsi, M.W. Barsoum, Two-dimensional nanoscrystals produced by exfoliation of Ti_3AlC_2, Adv. Mater. 23 (2011) 4248–4253, https://doi.org/10.1002/adma.201102306.
[23] Y. Gogotsi, B. Anasori, The Rise of MXenes, ACS Nano 23 (2019) 8491–8494, https://doi.org/10.1021/acsnano.9b06394.
[24] D. Wang, C. Zhou, A.S. Filatov, W. Cho, F. Lagunas, M. Wang, S. Vaikuntanathan, C. Liu, R.F. Klie, D.V. Talapin, Direct synthesis and chemical vapor deposition of 2D carbide and nitride MXenes, Science 379 (2023) 1242–1247, https://doi.org/10.1126/science.add9204.
[25] J.D. Gouveia, Á. Morales-García, F. Viñes, J.R.B. Gomes, F. Illas, MXenes *à la carte*: Tailoring the epitaxial growth alternating nitrogen and transition metal layers, ACS Nano 16 (2022) 12541–12552, https://doi.org/10.1021/acsnano.2c04029.
[26] B. Anasori, M.R. Lukatskaya, Y. Gogotsi, 2D metal carbides and nitrides (MXenes) form energy storage, Nat. Rev. Mat. 2 (2017) 16098, https://doi.org/10.1038/natrevmats.2016.98.
[27] G. Deysher, C.E. Shuck, K. Hantanasirisakul, N.C. Frey, A.C. Foucher, K. Maleski, A. Sarycheva, V.B. Shenoy, E.A. Stach, B. Anasori, Y. Gogotsi, Synthesis of Mo_4VAlC_4 MAX phase and two-dimensional Mo_4VC_4 MXene with five atomic layers of transition metals, ACS Nano 14 (2020) 204–217, https://doi.org/10.1021/acsnano.9b07708.
[28] V. Kamysbayev, A.S. Filatov, H. Hu, X. Rui, F. Lagunas, D. Wang, R.F. Klie, D. V. Talapin, Covalent surface modifications and superconductivity of two-dimensional metal carbide MXenes, Science 369 (2020) 979–983, https://doi.org/10.1126/science.aba8311.
[29] I. Persson, J. Halim, H. Lind, T.W. Hansen, J.B. Wagner, L.-Å. Näslund, V. Darakchieva, J. Palisitis, J. Rosen, P.O.Å. Persson, 2D transition metal carbides (MXenes) for carbon capture, Adv. Mater. 31 (2019) 1805472, https://doi.org/10.1002/adma.201805472.
[30] K. Arole, A. Micci-Barreca, S. Athavale, M. Tajedini, G. Raghuvaran, J. L. Lutkenhaus, M. Radovic, H. Liang, M.J. Green, Annealing $Ti_3C_2T_z$ MXenes to control surface chemistry and friction, ACS Appl. Mater. Interfaces 16 (2024) 6290–6300, https://doi.org/10.1021/acsami.3c18232.
[31] Á. Morales-García, A. Fernández-Fernández, F. Viñes, F. Illas, CO_2 abatement using two-dimensional MXene carbides, J. Mater. Chem. A 6 (2018) 3381–3385, https://doi.org/10.1039/C7TA11379J.
[32] M. López, Á. Morales-García, F. Viñes, F. Illas, Thermodynamics and kinetics of molecular hydrogen adsorption and dissociation on MXenes: Relevance to heterogeneously catalyzed hydrogenation reactions, ACS Catal. 11 (2021) 12850–12857, https://doi.org/10.1021/acscatal.1c03150.

[33] R. Morales-Salvador, J.D. Gouveia, Á. Morales-García, F. Viñes, J.R.B. Gomes, F. Illas, Carbon capture and usage by MXenes, ACS Catal. 11 (2021) 11248–11255, https://doi.org/10.1021/acscatal.1c02663.
[34] A. Kurlov, E.B. Deeva, P.M. Abdala, D. Lebedev, A. Tsoukalou, A. Comas-Vives, A. Fedorov, C.R. Müller, Exploiting two-dimensional morphology of molybdenum oxycarbide to enable efficient catalytic dry reforming of methane, Nat. Commun. 11 (2020) 4920, https://doi.org/10.1038/s41467-020-18721-0.
[35] H. Zhou, Z. Chen, A.Vidal López, E.D.íaz López, E. Lam, A. Tsoukalou, E. Willinger, D.A. Kuznetsov, D. Mance, A. Kierzkowska, F. Donat, P.M. Abdala, A. Comas-Vives, C. Copéret, A. Fedorov, C.R. Müller, Engineering the Cu/Mo_2CT_x (MXene) interface to drive CO_2 hydrogenation to methanol, Nat. Catal. 4 (2021) 860–871, https://doi.org/10.1038/s41929-021-00684-0.
[36] A. Jurado, Á. Morales-García, F. Viñes, F. Illas, Molecular mechanism and microkinetic análisis of the reverse water gas shift reaction heterogeneously catalyzed by the Mo_2C MXene, ACS Catal. 12 (2022) 15658–15667, https://doi.org/10.1021/acscatal.2c04489.
[37] J.D. Gouveia, Á. Morales-García, F. Viñes, F. Illas, J.R.B. Gomes, MXenes as promising catalysts for water dissociation, Appl. Catal. B: Environ. 260 (2020) 118191, https://doi.org/10.1016/j.apcatb.2019.118191.
[38] H. Zhou, Z. Chen, E. Kountoupi, A. Tsoukalou, P.M. Abdala, P. Florian, A. Fedorov, C.R. Müller, Two-dimensional molybdenum carbide 2D-Mo_2C as a superior catalyst for CO_2 hydrogenation, Nat. Commun. 12 (2021) 5510, https://doi.org/10.1038/s41467-021-25784-0.
[39] J.D. Gouveia, F. Viñes, F. Illas, J.R.B. Gomes, MXenes atomic layer stacking phase transitions and their chemical activity consequences, Phys. Rev. Mater. 4 (2020) 054003, https://doi.org/10.1103/PhysRevMaterials.4.054003.
[40] A. Jurado, Á. Morales-García, F. Viñes, F. Illas, Identifying the atomic layer stacking of Mo_2C MXene by probe molecule adsorption, J. Phys. Chem. C. 125 (2021) 26808–26813, https://doi.org/10.1021/acs.jpcc.1c07577.
[41] W. Sun, Y. Li, B. Wang, X. Jiang, M.I. Katsnelson, P. Korzhavyi, O. Eriksson, I. Di Marco, A new 2D monolayer BiXene, M_2C (M = Mo, Tc, Os), Nanoscale 8 (2016) 15753–15762, https://doi.org/10.1039/C6NR03602C.
[42] J.D. Gouveia, J.R.B. Gomes, The determining role of T_x species in the catalytic potential of MXenes: Water adsorption and dissociation on Mo_2CT_x, Catal. Today 424 (2023) 113848, https://doi.org/10.1016/j.cattod.2022.07.016.
[43] M. Keyhanian, D. Farmanzadeh, Á. Morales-García, F. Illas, Effect of oxygen termination on the interaction of first row transition metals with M_2C MXenes and the feasibility of single-atom catalysts, J. Mater. Chem. A 10 (2022) 8846–8855, https://doi.org/10.1039/d1ta10252d.
[44] G. Kresse, J. Futhmüller, Efficient iterative schemes for *ab initio* total-energy calculations using a plane-wave basis set, Phys. Rev. B 54 (1996) 11169, https://doi.org/10.1103/PhysRevB.54.11169.
[45] J.P. Perdew, K. Burke, M. Ernzerhof, Generalized gradient approximation made simple, Phys. Rev. Lett. 77 (1996) 3865–3868, https://doi.org/10.1103/PhysRevLett.77.3865.
[46] J.Rd.S. Politi, F. Viñes, J.A. Rodriguez, F. Illas, Atomic and electronic structure of molybdenum carbide phases: bulk and low Miller-index surfaces, Phys. Chem. Chem. Phys. 15 (2013) 12617–12625, https://doi.org/10.1039/C3CP51389K.
[47] S. Grimme, J. Antony, S. Ehrlich, S.A. Krieg, A consistent and accurate ab initio parametrization of density functional dispersion correction (DFT-D) for the 94 elements H-Pu, J. Chem. Phys. 132 (2010) 154104, https://doi.org/10.1063/1.3382344.
[48] J.P. Prates-Ramalho, J.R.B. Gomes, F. Illas, Accounting for van der Waals interactions between adsorbates and surfaces in density functional theory based calculations: selected examples, RSC Adv. 3 (2013) 13085–13100, https://doi.org/10.1039/C3RA40713F.
[49] P.E. Blöch, Project augmented-wave method. Phys. Rev. B 50 (1994) 17953, https://doi.org/10.1103/PhysRevB.50.17953.
[50] G. Henkelman, H. Jónsson, A dimer method for finding saddle points on high dimensional potential surfaces using only first derivatives, J. Chem. Phys. 111 (1999) 7010–7022, https://doi.org/10.1063/1.480097.
[51] F. Viñes, A. Calzada, P. Gamallo, Thermodynamic, kinetic and dynamic aspects of biogas upgrading using nano-engineered grazynes, J. CO_2 Util. 71 (2023) 102459, https://doi.org/10.1016/j.jcou.2023.102459.
[52] P. Nitoń, A. Zywociński, M. Fiałkowski, R. Hołyst, A "nano-windmill" driven by a flux of water vapour: A comparison to the rotating ATPase, Nanoscale 5 (2013) 9732–9738, https://doi.org/10.1039/c3nr03496h.
[53] S. Pogodin, N. López, A more accurate kinetic Monte Carlo approach to a monodimensional surface reaction: The interaction of oxygen with the RuO_2(110) surface, ACS Catal. 4 (2014) 2328–2332, https://doi.org/10.1021/cs500414p.
[54] J. Liu, M. Xu, T. Nordmeyer, F. Zaera, Sticking probabilities for CO adsorption on Pt(111) surfaces revisisted, J. Phys. Chem. 99 (1995) 6167–6175, https://doi.org/10.1021/j100016a062.
[55] B. Hellsing, B. Kasemo, S. Ljungström, A. Rosén, T. Wahnström, Kinetic model and experimental results for H_2O and OH production rates on Pt, Surf. Sci. 189-190 (1987) 851–860, https://doi.org/10.1016/S0039-6028(87)80521-6.
[56] R.W. McCabe, L.D. Schimidt, Binding states of CO and H_2 on clean and oxidized (111) Pt, Surf. Sci. 65 (1977) 189–209, https://doi.org/10.1016/0039-6028(77)90301-6.
[57] I.A.W. Filot, R.A. van Santen, E.J.M. Hensen, The optimally performing Fischer-Tropsch catalyst, Angew. Chem. 126 (2014) 12960–12964, https://doi.org/10.1002/ange.201406521.
[58] I.A.W. Filot, J.P. Broos, J.P.M. van Rijn, G.J.H.A. van Heugten, R.A. van Santen, E. J.M. Hensen, First-principles-based microkinetics simulations of synthesis gas conversion on a stepped Rhodium surface, ACS Catal. 5 (2015) 5453–5467, https://doi.org/10.1021/acscatal.5b01391.
[59] G.J. Kubas, R.R. Ryan, B.L. Swanson, P.J. Vergamini, H.J. Wasserman, Characterization of the first examples of isolable molecular hydrogen complexes, M$(CO)_3(PR_3)_2(H_2)$ (M = molybdenum or tungsten; R = Cy or isopropyl). Evidence for a side-on bonded dihydrogen ligand, J. Am. Chem. Soc. 106 (1984) 451–452, https://doi.org/10.1021/ja00314a049.
[60] M. Manadé, F. Viñes, A. Gil, F. Illas, On the H_2 interactions with transition metal adatoms supported on graphene: a systematic density functional study, Phys. Chem. Chem. Phys. 20 (2018) 3819–3830, https://doi.org/10.1039/C7CP07995H.
[61] M. Figueras, A. Jurado, Á. Morales-García, F. Illas, Bulk (in)stability as a possible source of surface reconstruction, Phys. Chem. Chem. Phys. 22 (2020) 19249–19253, https://doi.org/10.1039/D0CP03819A.
[62] M.D. Porosoff, X. Yang, J.A. Boscoboinik, J.G. Chen, Molybdenum carbide as alternative catalysts to precious metals for highly selective reduction of CO_2 to CO, Angew. Chem., Int. Ed. 53 (2014) 6705–6709, https://doi.org/10.1002/anie.201404109.
[63] X. Zhang, X.B. Zhu, L.L. Lin, S.Y. Yao, M.T. Zhang, X. Liu, X. Wang, Y.-W. Li, C. Shi, D. Ma, Highly dispersed copper over β-Mo_2C as an efficient and stable catalyst for the reverse water gas shift (RWGS) reaction, ACS Catal. 7 (2017) 912–918, https://doi.org/10.1021/acscatal.6b02991.
[64] D. Dolz, R. De Armas, P. Lozano-Reis, Á. Morales-García, F. Viñes, R. Sayós, F. Illas, Understanding the reverse water gas shift reaction over Mo_2C MXene catalyst: A holistic computational analysis, ChemCatchem 16 (2024) e202400122, https://doi.org/10.1002/cctc.202400122.